

BODIPY-Based Photothermal Agents with Excellent Phototoxic Indices for Cancer Treatment

Lukas Schneider,^{||} Martina Kalt,^{||} Samuel Koch, Shanmugi Sithamparanathan, Veronika Villiger, Johann Mattiat, Flavia Kradolfer, Ekaterina Slyshkina, Sandra Luber, Mathias Bonmarin, Caroline Maake, and Bernhard Spingler*



Cite This: *J. Am. Chem. Soc.* 2023, 145, 4534–4544



Read Online

ACCESS |



Metrics & More

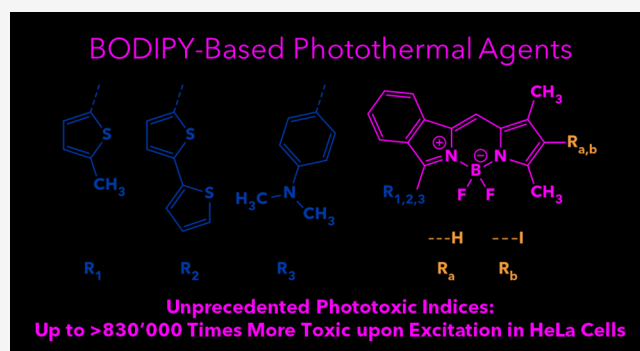


Article Recommendations



Supporting Information

ABSTRACT: Here, we report six novel, easily accessible BODIPY-based agents for cancer treatment. In contrast to established photodynamic therapy (PDT) agents, these BODIPY-based compounds show additional photothermal activity and their cytotoxicity is not dependent on the generation of reactive oxygen species (ROS). The agents show high photocytotoxicity upon irradiation with light and low dark toxicity in different cancer cell lines in 2D culture as well as in 3D multicellular tumor spheroids (MCTSs). The ratio of dark to light toxicity (phototoxic index, PI) of these agents reaches striking values exceeding 830,000 after irradiation with energetically low doses of light at 630 nm. The oxygen-dependent mechanism of action (MOA) of established photosensitizers (PSs) hampers effective clinical deployment of these agents. Under hypoxic conditions (0.2% O₂), which are known to limit the efficiency of conventional PSs in solid tumors, photocytotoxicity was induced at the same concentration levels, indicating an oxygen-independent photothermal MOA. With a PI exceeding 360,000 under hypoxic conditions, both PI values are the highest reported to date. We anticipate that small molecule agents with a photothermal MOA, such as the BODIPY-based compounds reported in this work, may overcome this barrier and provide a new avenue to cancer therapy.



INTRODUCTION

In the past couple of decades, photodynamic therapy (PDT) has become a widely used therapeutic method for the treatment of a variety of premalignant and malignant diseases.^{1–3} PDT conventionally involves the application of a photosensitizer (PS) that is activated by light in the tissue to be treated. This method has many potential applications due to the advantages it presents as a non- or minimally invasive therapy. PDT does not exhibit cumulative toxicity, and its activation can be controlled both spatially and temporally. The adjustable light used, as well as the short diffusion radius of the emerging reactive oxygen species (ROS), minimizes the damage to surrounding healthy tissue.^{4,5}

The mechanism of action (MOA) consists of the PS-mediated generation of ROS from its first excited triplet state.⁶ The generated ROS involves singlet oxygen (¹O₂) via the type II mechanism, or radical species such as hydroxyl radicals (OH[•]) and superoxide anions (O₂^{•-}) via the type I mechanism.⁷ Both mechanisms depend on molecular oxygen (³O₂) in the tissue, leading to reported clinical resistance under hypoxia. This MOA is a major drawback as solid tumors are invariably less well-oxygenated than nonmalignant tissue.^{8–12}

Alternative MOAs to the type I and type II pathways have been reported in literature despite a lack of consensus regarding the definition of oxygen-independent mechanisms.^{10,13} A modified type I mechanism, called type III, has been described based on an interaction between the PS in its first excited triplet state and doublet free radicals with diffusion-controlled rate constants.^{14–19} Other reports of oxygen-independent mechanisms involve the generation of toxic photoproducts from upper excited triplet states,²⁰ photoinduced electron transfers leading to cycloaddition reactions,^{21,22} and structural changes upon excitation that allow binding to intracellular targets.^{10,18} These properties currently preclude therapeutic deployment. Additional agents for phototherapy undergoing photoredox catalysis have been reported recently.^{23,24}

Furthermore, phototherapeutic treatment methods have emerged based on photothermal therapy (PTT). PTT applies

Received: November 2, 2022

Published: February 13, 2023



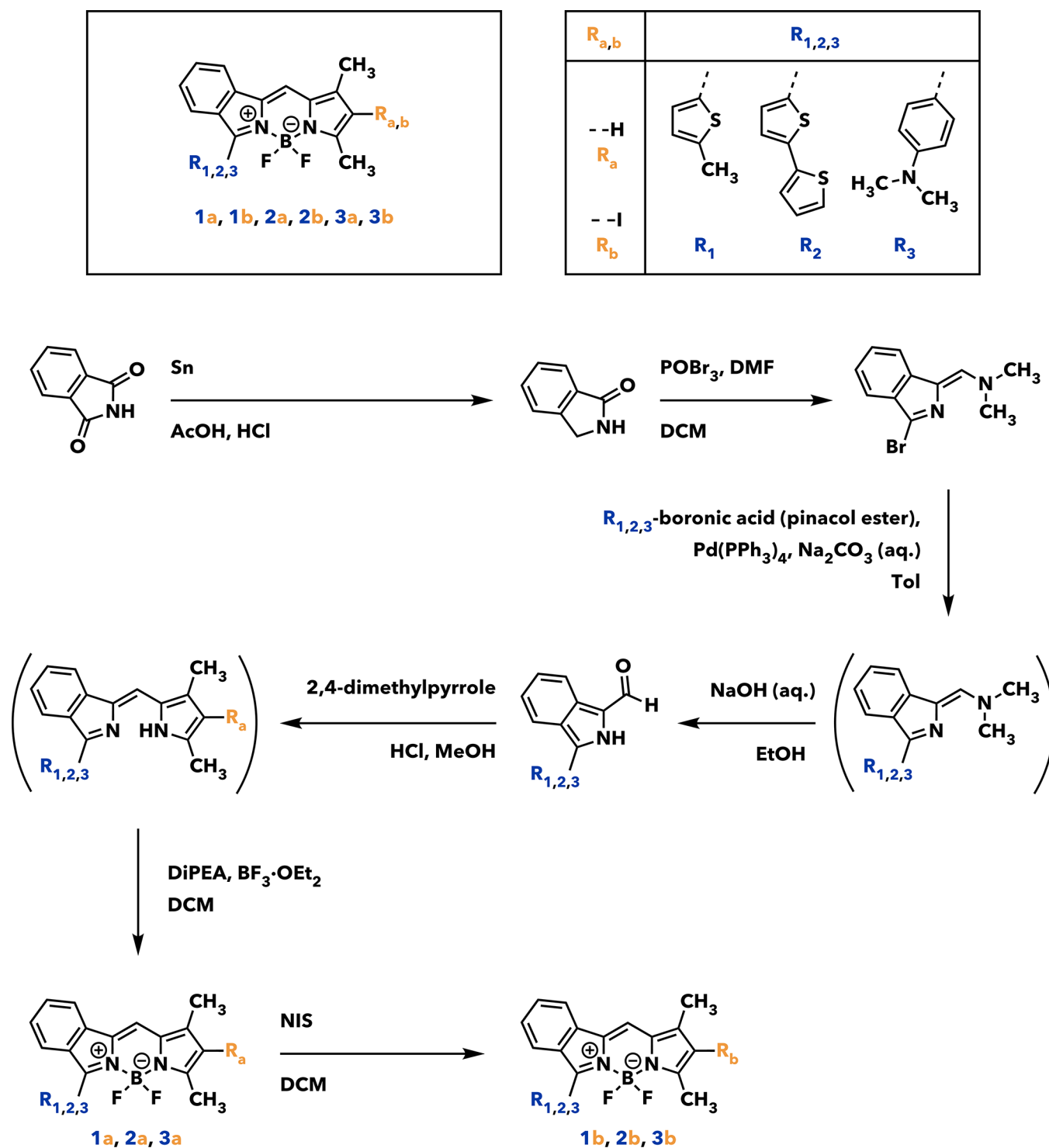


Figure 1. Synthetic pathway toward the common precursor compounds as well as BODIPYs 1a, 1b, 2a, 2b, 3a, and 3b. The corresponding crystal structures are shown in the Supporting Information (Figure S1). The detailed experimental procedures are reported in the Supporting Information (sections S1–S5). Intermediates shown in brackets were not isolated.

functional biomedical and bioactive nanomaterials activated by light in the near-infrared (NIR) range to eliminate tumor cells via the generation of heat upon irradiation.^{25–28} Despite the many advantages of PTT, drawbacks concerning biocompatibility, biodegradation, long-term toxicity, and threats of these nanomaterials to the environment remain unresolved.²⁵ Small molecules rather than nanomaterials have been employed for PTT; however, all the previous approaches required a

nanoprecipitation step, again precluding straightforward use in a biological context.^{29–31}

Here, we report six novel metal-free BODIPY-based (boron-dipyrromethene) agents that are able to undergo an oxygen-independent photothermal MOA upon excitation with small doses of light in the visible range. The compounds are easily accessible and have phototoxic indices (PIs), the ratio of dark to light toxicity,^{32–34} of over 830,000 in cancer cells under

Table 1. Photophysical Properties of 1a, 1b, 2a, 2b, 3a, and 3b^a

Compd	Absorption λ_{\max} (nm), log(ϵ)	Emission λ_{\max} (nm)	Φ_{Δ}	Φ_{F}	τ_{F} (ns) ^b	τ_{T} (ns) ^b	Φ_{d}
1a	589, 4.69	619	0	0.82 \pm 0.06	13.6	—	Photostable (>2 h)
1b	598, 4.70	633	0.26 \pm 0.05	0.50 \pm 0.03	4.69	120	(6.5 \pm 0.6) $\times 10^{-6}$
2a	608, 4.69	651	0	0.43 \pm 0.01	5.40	—	(7.8 \pm 0.5) $\times 10^{-5}$
2b	619, 4.65	656	0.15 \pm 0.01	0.33 \pm 0.04	3.45	147	(6.4 \pm 0.3) $\times 10^{-6}$
3a	588, 4.65	626	0	0.025 \pm 0.001	3.72	—	Photostable (>2 h)
3b	596, 4.55	639	0	0.010 \pm 0.001	3.22	—	Photostable (>2 h)

^aUV–vis absorption measured in MeOH-*d*₄; Fluorescence emission measured in MeOH-*d*₄; Φ_{Δ} measured in MeOH-*d*₄; Φ_{F} measured in MeOH; τ_{F} measured in MeOH; τ_{T} measured in MeOH; Φ_{d} measured in DMF. Additional UV–vis absorption, and fluorescence emission spectra and data measured in H₂O, MeOH, DCM, and toluene are reported in the Supporting Information. ^bThe estimated errors for the values reported are 10%.

normoxic conditions and over 360,000 under hypoxic conditions (0.2% O₂). BODIPY-based compounds have favorable properties, being easily accessible small molecules that are excitable with tissue-penetrating red light at 630 nm. In contrast to conventional PTT systems, they can be applied in solution and do not require additional additives or the nanoprecipitation step prior to application. We anticipate that their toxicity to cancer cells through local light-to-heat conversion might help to overcome the enormous drawback of hypoxia resistance in PDT as well as the toxicity issues of nanomaterials in PTT.

RESULTS

Characterization. All compounds are based on an asymmetric BODIPY-based structure³⁵ with an extended π -system and varying bathochromically shifting moieties. BODIPYs are known for their high chemical stability and molar extinction coefficients, and their photophysical properties as well as their solubility can be fine-tuned by countless possibilities of synthetic functionalization.³⁶ Therefore, they are promising candidates for light-induced cancer therapy. Compounds 1a, 2a, and 3a were synthesized according to the synthetic pathway (Figure 1); their syntheses are described in detail in the Supporting Information (sections S1–S5). Compounds 1b, 2b, and 3b (Figure 1) were obtained after monoiodination of compounds 1a, 2a, and 3a, respectively, and contain an additional iodine atom to induce a heavy-atom effect and higher triplet state quantum yields.^{37,38} All compounds were characterized as described in the Supporting Information (sections S1–S5) by spectroscopic and analytical data including UV–vis, fluorescence emission, IR, NMR, and mass spectroscopy, liquid chromatography, single crystal X-ray analysis (sections S1–S6, Figure S1), elemental analysis, and partition constant determination (section S7, Table S1).

Photophysical measurements were carried out for all six compounds. The singlet oxygen quantum yields (Φ_{Δ}) (Table 1, Table S2) of 1a, 1b, 2a, 2b, 3a, and 3b were determined by applying light at a wavelength of 630 nm (Figure S3) based on a direct method (section S9).^{36,39–42} Fluorescence quantum yields (Φ_{F}) (Table 1, Table S3) of 1a, 1b, 2a, 2b, 3a, and 3b were determined as described in section S10. All compounds are highly fluorescent in aprotic solvents like DCM and toluene, and nonfluorescent in H₂O, and all compounds except 3a and 3b are highly fluorescent in the protic solvent MeOH with Φ_{F} values ranging from 0.33 to 0.82, while the protic character of MeOH quenches the fluorescence emission of 3a and 3b to $\Phi_{\text{F}} \leq 0.03$. The fluorescence lifetimes (τ_{F}) (Table 1, Table S4) of all compounds have been determined in MeOH (section S11), resulting in τ_{F} values in the range 3.22 to 13.6 ns. The absorption maximum of all studied compounds is in the range between 588

and 619 nm in MeOH, and the fluorescence emission maximum between 619 and 656 nm. In MeOH, DCM, and toluene, all compounds exhibit a rather sharp absorption maximum, while in H₂O the absorption peak is very broad with distinctly lower extinction coefficients compared to the other solvents. The addition of the iodine atom to the pyrrolic position bathochromically shifts the absorption maximum between 8 and 11 nm compared to the noniodinated analogue compound. The compound pair 2a and 2b exhibit their absorption maximum at the longest wavelengths due to the presence of a second thiophene unit that is contributing to the photochemical system of the compounds. Noniodinated compounds 1a, 2a, and 3a do not generate ¹O₂, while the iodine-containing derivatives 1b and 2b show a low Φ_{Δ} of 0.26 \pm 0.05 and 0.15 \pm 0.01, respectively, in contrast to 3b that does not generate ¹O₂ at all in MeOH-*d*₄. BODIPY-based compounds containing a *N,N*-dimethylaniline moiety as in the case of 3b are known for undergoing intramolecular charge transfers (ICTs) in the nonprotonated state upon irradiation that quenches the ¹O₂ generation.^{36,43–45} This correlates with the triplet state lifetimes (τ_{T}) (Table 1, Table S5) determined as described in section S12. While a τ_{T} of 120 ns was measured for 1b, and a τ_{T} of 147 ns for 2b, no triplet state was detected for the third compound of the iodinated series, 3b. Furthermore, no triplet state could be detected in the case of all noniodinated compounds 1a, 2a, and 3a, which is also in line with the observed Φ_{Δ} values. The ability to generate ¹O₂ (type II mechanism) and the ability to generate hydroxyl radicals ([•]OH), superoxide anions (O₂^{•-}) and/or other ROS (type I mechanism) was investigated with the corresponding chemical sensors⁴⁶ as described in section S13 (graphs shown in Figure S9). Compared to the standard methylene blue (MB), only small amounts of ROS were detected in the case of 1a, 1b, 2a, 2b, 3a, and 3b after irradiation with light at 630 nm (Figure S8) for 40 min (total applied energy = 5.0 J/cm²). This suggests that the generation of ROS is not the primary mechanism to induce photocytotoxicity.

The first two excited singlet (S_x) and triplet (T_x) states of 1a, 1b, 2a, 2b, 3a, and 3b were calculated at the TDDFT level using geometry optimized structures (section S14). The BLYP exchange–correlation functional^{47,48} was employed for the geometry optimizations and the TDDFT calculations. Additionally, TDDFT calculations were carried out using the B3LYP hybrid exchange–correlation functional^{48–50} (results shown in Table S6). Visualizations of the calculated natural transition orbitals (NTOs)⁵¹ for the first excited singlet state (S₁) (section S15) provide an intuitive particle-hole picture after the immediate absorption (results shown in Figure S10). The results indicate that the long-lived first excited triplet state (T₁) is energetically accessible for all six compounds. As the calculations were carried out for optimized ground state

structures, the calculated energies correspond to vertical excitation energies. In order to obtain insight into the actual photochemical processes involved, nonadiabatic dynamics would be required, and the computational cost of which goes beyond the scope of this work. Additional calculations performed using the COSMO solvation model⁵² to account for solvation effects indicated comparable results (results shown in Table S7).

The photostability of all compounds was determined (section S16) by measuring the photobleaching quantum yields (Φ_d) (Table 1, Table S8). Compounds **1a**, **3a**, and **3b** were photostable under the applied conditions in DMF, while **1b**, **2a**, and **2b** showed small Φ_d in comparison to zinc phthalocyanine (**ZnPc**) ($\Phi_d = 0.23 \times 10^{-4}$ in DMF⁵³).

Photocytotoxicity. The photocytotoxicity of **1a**, **1b**, **2a**, **2b**, **3a**, and **3b** (Table 2, Figure S11) was studied as described in

Table 2. IC₅₀ Values of **1a, **1b**, **2a**, **2b**, **3a**, and **3b** in the Dark and upon Irradiation, and the Corresponding PI Values^a**

Compd	IC ₅₀ (irradiation, μM)	IC ₅₀ (dark, μM)	PI
1a	0.730 \pm 0.004	>5000	>6800
1b	0.0060 \pm 0.0003	>5000	>830,000
2a	0.130 \pm 0.003	1250 \pm 88	9600
2b	0.0350 \pm 0.0009	2070 \pm 269	59,000
3a	0.56 \pm 0.04	1330 \pm 123	2400
3b	0.032 \pm 0.002	2160 \pm 139	68,000

^aCompound **1b** is the most efficient compound with an IC₅₀ value of 0.0060 \pm 0.0003 μM upon light irradiation, >5000 μM in the dark and a PI of >830,000.

sections S17–S19, the light dose dependency (Figure S14) and time-dependent cellular uptake (Figure S15) were determined as described in sections S20–S21. HeLa human cervical cancer cells were treated either with the compounds or without compounds as treatment control, and further irradiated with light of 630 nm (Figure S8) for 40 min corresponding to an energy dose of 5.0 J/cm². Despite the high Φ_F values, low Φ_Δ values, and low levels of generated ROS, **1a**, **1b**, **2a**, **2b**, **3a**, and **3b** showed high photocytotoxicity when exposed to this low total energy dose. The IC₅₀ (half maximal inhibitory concentration) values of all iodinated compounds are in the one- or two-digit nanomolar range. As expected, they are distinctly lower than for all noniodinated compounds. The presence of a T₁ state, based on the measurable τ_T , does not correlate with the observed photocytotoxicities, and the noniodinated compounds **1a**, **2a**, and **3a** as well as the iodinated compound **3b** show photocytotoxicity. All compounds furthermore show very low toxicity in the dark with IC₅₀ values up to >5 mM. The most interesting noniodinated/iodinated compound pair **1a** and **1b** is nontoxic in the dark in HeLa cells (IC₅₀ >5 mM), while **1a** as the noniodinated compound has an IC₅₀ value of 0.730 \pm 0.004 μM upon irradiation and **1b** as the iodinated compound has an IC₅₀ value of 0.0060 \pm 0.0003 μM upon irradiation. This is equal to a PI of over 830,000 for **1b**. This is, to the best of our knowledge, the highest PI value reported for any photosensitizer. Photocytotoxicity determinations of **1a** and **1b** in other cell lines such as in the A2780 human ovarian cancer cell line (Table S9, Figure S12) and MRC-5 human fetal lung fibroblast cell line (Table S10, Figure S13) showed similar photochemical and phototoxic properties.

Photocytotoxicity and growth-inhibiting properties (Figure 2, Table S11, Figure S16) of the most promising compound **1b** in

HeLa 3D multicellular tumor spheroids (MCTSs), which are known to simulate the conditions found in clinically treated tumors,^{54,55} have been determined as described in sections S22–S24. The photocytotoxicity assay with **1b** was carried out under analogous conditions to those used for determining photocytotoxicity in HeLa cell monolayers using light with a wavelength of 630 nm (Figure S8) and an irradiation time of 40 min corresponding to an energy dose of 5.0 J/cm². IC₅₀ values for **1b** in HeLa MCTSs have been determined to be 0.12 \pm 0.04 μM after light exposure and >1660 μM in the dark, resulting in a PI of >13,800. This underlines the photocytotoxic potency of **1b** observed in the different cell lines in a simple model system with tumor-like conditions.

The growth-inhibiting properties of **1b** in HeLa MCTSs were measured before and after treatment with **1b**. MCTSs treated with **1b** and irradiated with light were compared to three control conditions: MCTSs treated with **1b** and kept in the dark, MCTSs treated with the solvent vector only and kept in the dark, and MCTSs treated with the solvent vector upon irradiation with light. All three control conditions led to linear MCTS growth during the observation window with an average MCTS size of 181% on day five compared to the initial size. MCTSs treated with **1b** and subsequent irradiation with light of 630 nm started dissolving on day three, which is visible as an optical “inflation” of the MCTSs to 233% of the initial size followed by a steady decrease in size. This shows that **1b** is not just decreasing the growth rate of the MCTSs like cisplatin,⁴² but actively destroying them upon irradiation. The observed change in size of the MCTSs is shown in micrographs of single MCTSs over time (Figure 2a), as well as MCTS size relative to time (Figure 2b).

Because MCTSs also simulate tumor hypoxia and proliferation gradients to the center,^{54,55} the observed effectivity in HeLa MCTSs indicated a possible efficiency under hypoxic conditions. To test this hypothesis, the photocytotoxicity determination for compounds **1a** and **1b** in monolayer HeLa cells was repeated under hypoxic conditions (Table 3, Figure S17) as described in section S25. Both **1a** and **1b** proved to be highly effective in HeLa cells under hypoxic conditions while being treated and excited analogous to conditions used to test phototoxicity in HeLa cells under normoxic conditions. IC₅₀ values in the dark were, as expected, slightly lower under hypoxic conditions with values >2500 μM for both **1a** and **1b**. While the IC₅₀ value upon excitation with light of the noniodinated compound **1a** increased to 1.87 \pm 0.08 μM , the IC₅₀ value of the iodinated compound **1b** remained virtually unchanged with a value of 0.0069 \pm 0.0003 μM , showing that **1b** is highly photocytotoxic not only under normoxic conditions but also under hypoxic conditions as prevalent in the majority of solid tumors^{9,56} that can lead to hypoxic drug resistance⁸ especially in the case of PDT agents.¹¹

Mechanism of Action. In order to determine the cellular uptake pathway of compound **1b**, we inhibited specific uptake pathways in HeLa cells (section S26). Different uptake pathways were blocked by preincubation with a cationic transporter, metabolic, and endocytotic inhibitors.^{54,57–59} None of the blocked pathways showed an impact on the uptake efficiency of **1b** (Figure S18). Compared to the standard setting, the uptake of **1b** is 26% lower at low temperature (4 °C). This indicates that **1b** is primarily taken up by passive diffusion. Intracellular ROS levels upon irradiation after exposure to **1b** were measured (section S26). Compared to **MB** only a minor fraction of the cells tested were ROS-positive after the application of **1b** and

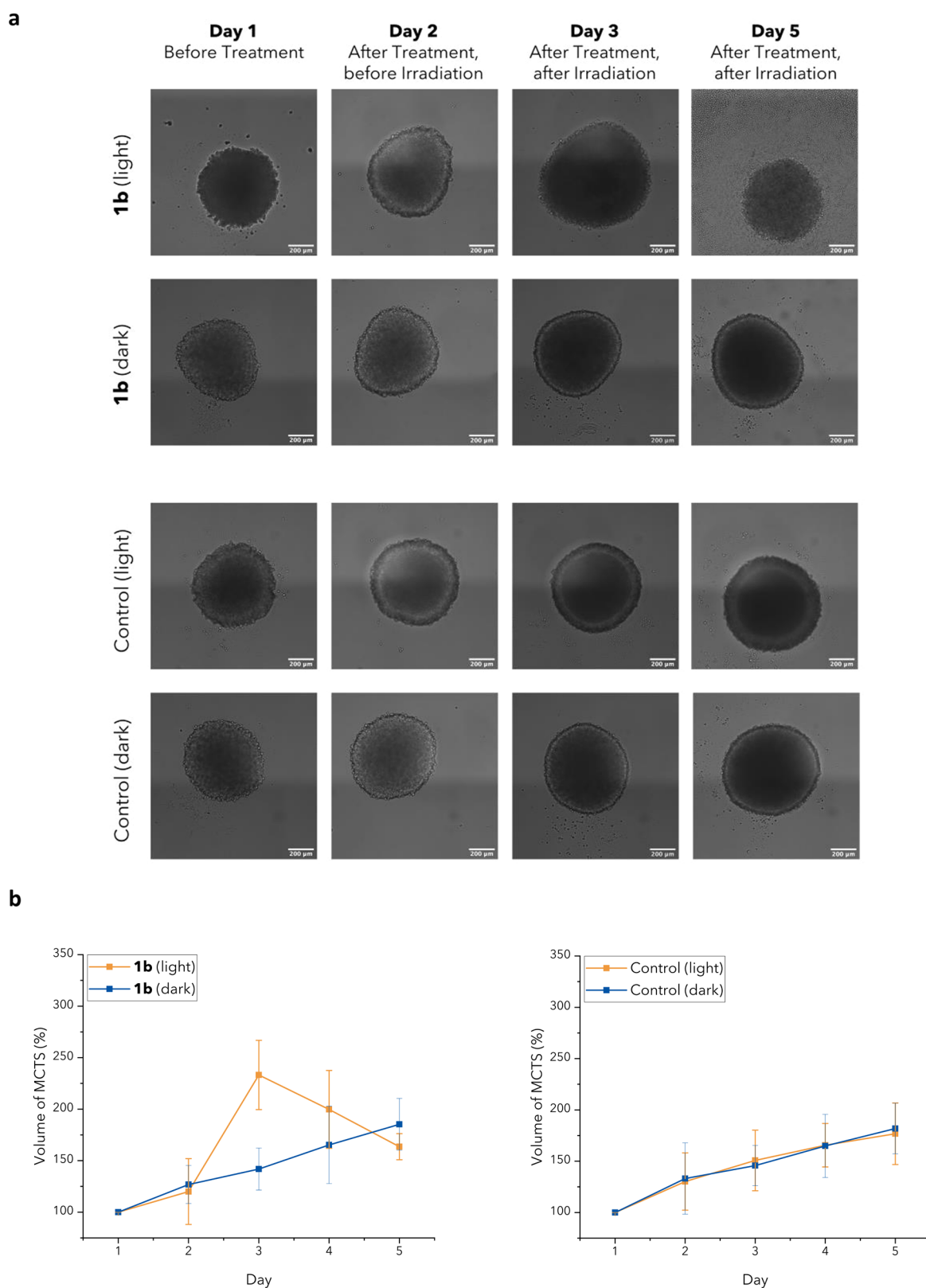


Figure 2. (a) Micrographs of 3D HeLa multicellular tumor spheroids (MCTSs) taken over 5 days (scale bars = 200 μm). (b) Monitored growth of 3D HeLa MCTSs over 5 days compared to the initial size. MCTSs were treated either with **1b**, or the solvent vector (Control), and irradiated with light of 630 nm (light), or kept in the dark (dark).

subsequent irradiation (Figure S19). This is in line with the observation of low levels of different kinds of ROS generated by **1b** in solution (Figure S9). Together with the observed high photocytotoxicity under hypoxic conditions, these low ROS

levels indicate that an oxygen-independent MOA is the major cytotoxic pathway. Micrographs visualizing generated intracellular ROS (Figure 3b, Figure S20) were taken (section S28),

Table 3. Photocytotoxicities and Dark Toxicities as well as the PIs of **1a and **1b** in HeLa Cells under Hypoxic Conditions (0.2% O₂, 630 nm, 5.0 J/cm²)**

Compd	IC ₅₀ (irradiation, μM)	IC ₅₀ (dark, μM)	PI
1a	1.87 ± 0.08	>2500	>1300
1b	0.0069 ± 0.0003	>2500	>360,000

and the results are in line with the intracellularly measured ROS levels.

Intracellular localization of **1a** and **1b** was investigated in HeLa cells (Figure 3a, Figure S21) with different dyes for cell organelle staining (section S29). Both **1a** and **1b** are observable as distinct spherical fluorescent spots and seem to behave similarly after being taken up in the cell. Neither compound colocalized with markers for the nucleus, the mitochondria, the Golgi apparatus, the endoplasmic reticulum, lysosomes, or peroxisomes. This indicates that both **1a** and **1b** form local clusters in the cytosol of HeLa cells without specific accumulation in any of the tested cell organelles.

Next, we tested the ability of **1b** to disrupt the mitochondrial membrane potential (MMP) in HeLa cells (section S30). Disruption of the MMP indicates an effect on the mitochondrial electron transfer chain and a failure of mitochondrial function, and is associated with an apoptotic or necrotic cell death mechanism.^{60,61} The MMP of HeLa cells was not disrupted after the application of **1b** in the concentration range 0.5 nM–0.5 μM in the dark, while a clear disruption is visible for **1b** upon application and subsequent irradiation from an applied concentration of 5.0 μM onward (Figure S22). This concentration is in line with the observed IC₅₀ value of **1b** in HeLa cells (Table 2). Visualization of MMP disruption by **1b** (Figure 3c, Figure S23) was carried out with different concentrations of **1b** in the dark, and upon irradiation (section S31). The results were consistent with the MMP disruption experiments.

To investigate the cell death pathway induced by **1b** upon irradiation further, an annexin V/propidium iodide assay in HeLa cells (Figure S24) was applied (section S32). This assay shows through changes in the plasma membrane integrity/permeability if cells are viable, apoptotic, or necrotic.^{62,63} The observed staining of HeLa cells with the isothiocyanate–annexin V conjugate is in line with the results obtained in the MMP disruption experiment (Figure S22). The cells additionally showed a fluorescent signal upon costaining with propidium iodide, which indicates a necrotic cell death mechanism since the presence of an intact plasma membrane would prevent propidium iodide from entering early apoptotic cells.⁶⁴ To exclude a photoredox-based MOA^{23,24} of **1b** in HeLa cells, the intracellular NAD⁺/NADH levels (Figure S25) and GSH/GSSG levels (Figure S26) of HeLa cells treated with **1b** upon irradiation were determined (sections S33–S34). No relevant changes in levels of either NAD⁺/NADH or GSH/GSSG are observed upon treatment with **1b** and subsequent irradiation in the range size of its IC₅₀ value. This shows that the MOA of **1b** in HeLa cells is not photoredox-induced.

To investigate the clusters formed by **1a** and **1b** that were observed in the intracellular localization experiments (Figure 3a), dynamic light scattering (DLS) was used (section S35) to examine whether aggregates of **1a** and **1b** form in the cellular environment (Table S12). Both **1a** and **1b** form aggregates in DMEM, which was used as a model system to test the aggregation behavior since it is the most common cell medium

for culturing mammalian cells.⁶⁵ For **1a** an aggregate size distribution of 122 ± 46 (31.4%), 6 ± 2 (51.3%), and 0.65 ± 0.04 (31.4%) nm was observed; for **1b** a size distribution of 4620 ± 819 (2.0%), 86 ± 33 (79.7%), and 3.8 ± 0.6 (18.3%) nm was observed. Aggregates formed by **1b** in the cell could give rise to a photothermal MOA of **1b** upon irradiation that triggers a cell death pathway through the local light-to-heat generation, similar to nanomaterials applied in PTT.²⁵ To test this hypothesis, the specific absorption rates (SARs), which are used in literature to experimentally quantify the heating efficiency of compounds,⁶⁶ of **1a** and **1b** were determined (Figure S27) using a lock-in thermal imaging setup (LIT) measuring the corresponding amplitude (section S36). Compound **1b** shows overall higher SAR values compared to **1a** (Table 4, Figure 4), which is in line with the behavior of the compounds regarding photocytotoxicity (Table 2). While the SAR values of **1a** lie in a compound concentration range of 6.25 μM to 100 μM slightly below 4500 W/g at 6.25 μM and decrease with increasing concentrations, the ones of **1b** show a similar concentration dependency, however at much higher values ranging from around 27,600 W/g at 6.25 μM to 5800 W/g at 100 μM. This shows the SARs of both **1a** and **1b** increase as expected with lower concentrations, most likely due to the higher solvated state of individual molecules, indicating that at compound concentrations present in HeLa cells a photothermal MOA emerging from locally formed clusters of **1b** is conceivable. The SAR values measured for **1a** and **1b** were benchmarked against the commercially available molecular photothermal agent indocyanine green (ICG)⁶⁷ (Figure S28, Table S13). ICG shows slightly lower SAR values compared to **1b** around 16,200 W/g and 20,100 W/g depending on the wavelength of excitation; however, its biological effectiveness is distinctly lower since the optimal concentration in HeLa cells to observe a phototoxic effect is 94 μM.⁶⁸ In comparison, IC₅₀ values of the reported BODIPY-based agents are as low as 0.0060 ± 0.0003 μM upon excitation in HeLa cells.

DISCUSSION

The presence of molecular oxygen in the tissue to be treated plays a crucial role in the MOA of PDT, making this approach ineffective in tumors surrounded by necrotic tissue or dense tumor masses.⁶⁹ Different strategies, such as the application of oxygen vehicles, have been proposed to overcome the barrier posed to PDT by the hypoxic environment in solid tumors.⁷⁰ This environment arises from the abnormal structure of the microvessels and tumor microenvironment that leads to ineffective blood distribution,⁷⁰ and leads to low oxygen levels that limit PDT.⁷¹ PTT is one photoinduction strategy that would circumvent this limitation, since the therapeutic efficiency of PTT is not affected by oxygen levels.⁷² It is even possible that PDT could be combined with PTT to produce a synergistic effect, even in solid tumors.^{72,73}

Here, we examined small molecules that can act as photothermal agents. With only minute levels of ROS generated upon irradiation, as detected by applied ROS sensors (Figure S9) in PBS as well as intracellularly in HeLa cells (Figures 3b, S19–S20), the main MOA of **1a**, **1b**, **2a**, **2b**, **3a**, and **3b** is photothermal (Table 4, Figure 4) and bypasses the limitation of PDT. A particularly interesting insight comes from examination of the compound pair **3a** and **3b**. While both compounds show energetically accessible first excited triplet state (T₁) energy levels based on the results from TDDFT simulations (Tables S7 and S8), no ¹O₂ production was observed (Table 1), which is in

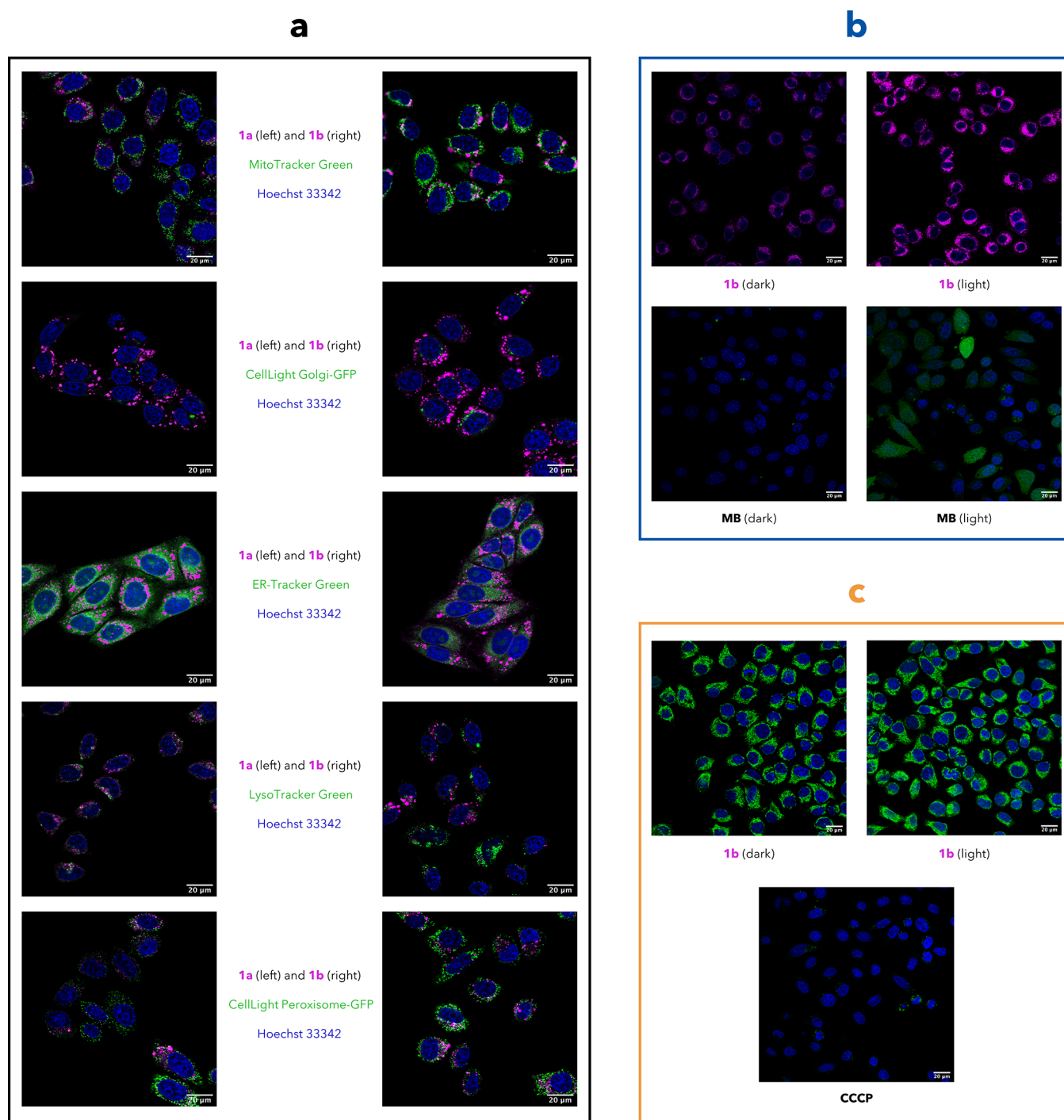


Figure 3. (a) Merged intracellular localization images of **1a** and **1b** (shown in purple, $\lambda_{\text{ex/em}} = 590/600\text{--}700$ nm) in HeLa cells visualized together with the nucleus (shown in blue, Hoechst 33342: $\lambda_{\text{ex/em}} = 405/450\text{--}495$ nm) and mitochondria (shown in green, MitoTracker Green FM: $\lambda_{\text{ex/em}} = 488/500\text{--}550$ nm), Golgi apparatus (shown in green, CellLight Golgi-GFP, BacMam 2.0: $\lambda_{\text{ex/em}} = 488/500\text{--}550$ nm), endoplasmic reticulum (shown in green, ER-Tracker Green: $\lambda_{\text{ex/em}} = 504/514\text{--}550$ nm), lysosomes (shown in green, LysoTracker Green DND-26: $\lambda_{\text{ex/em}} = 504/514\text{--}550$ nm), or peroxisomes (shown in green, CellLight Peroxisome-GFP, BacMam 2.0: $\lambda_{\text{ex/em}} = 488/500\text{--}550$ nm). Images of individual stains are shown in Figure S21. No colocalization with any of the tested organelles is observable for **1a** or **1b**. (b) Micrographs showing no generated intracellular ROS (shown in green as DCF emission) for **1b** (shown in purple) after irradiation, and intracellular ROS generated by MB after irradiation (positive control). The whole set of done experiments is shown in Figure S20. (c) Micrographs showing no MMP disruption for **1b** after irradiation (emission from the MAK147 dye is shown in green) and MMP disruption induced by CCCP (positive control). The whole set of done experiments is shown in Figure S23.

line with the nonexistent T_1 state observed in the τ_T measurements (Table 1). Despite this, both compounds show high photocytotoxicity (Table 2).

The oxygen-independent MOA of the most effective compound, **1b**, was demonstrated upon irradiation under

hypoxia in HeLa cells (Table 3, Figure S17), where virtually no change in the high effectivity was observed. Additionally, a high efficiency of **1b** in HeLa MCTS was confirmed upon irradiation (Figure 2, Table S11, Figure S16), underlining the effectivity of the reported agents. Despite the benefits of the

Table 4. Measured Amplitude A , Heating Slope β , and Calculated Specific Absorption Rates (SAR) for **1a and **1b** Based on Measurements by Lock-in Thermal Imaging (LIT)**

Compd	Concn (μM)	Amplitude A (K) $\times 10^{-3}$	Heating Slope β (K/s) $\times 10^{-2}$	SAR (W/g) $\times 10^3$
1a	6.25	0.38 ± 0.01	0.47 ± 0.01	4.4 ± 0.1
1a	12.5	0.35 ± 0.01	0.44 ± 0.02	2.09 ± 0.07
1a	25	0.36 ± 0.01	0.45 ± 0.01	1.06 ± 0.03
1a	50	0.34 ± 0.03	0.43 ± 0.03	0.50 ± 0.04
1a	100	0.41 ± 0.02	0.51 ± 0.02	0.30 ± 0.01
1b	6.25	3.14 ± 0.05	3.94 ± 0.06	27.6 ± 0.4
1b	12.5	3.2 ± 0.1	4.1 ± 0.1	14.3 ± 0.5
1b	25	4.3 ± 0.2	5.4 ± 0.3	9.4 ± 0.5
1b	50	7.3 ± 0.4	9.2 ± 0.5	8.1 ± 0.5
1b	100	10.5 ± 1.0	13.2 ± 1.32	5.8 ± 0.6

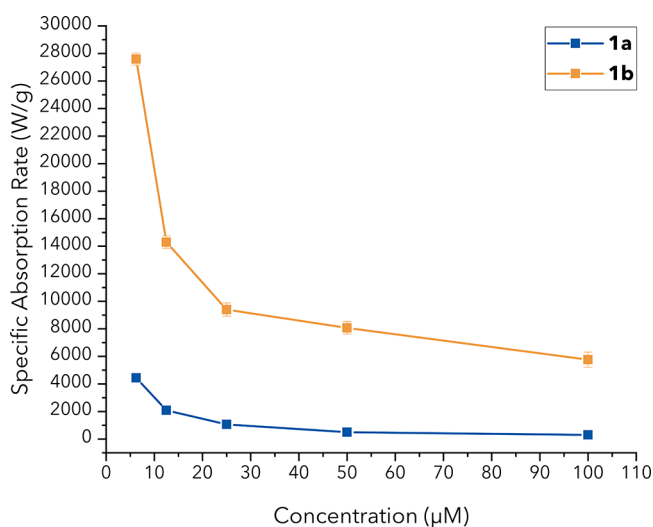


Figure 4. Specific absorption rates (W/g) of **1a** and **1b** plotted versus the concentration. A clear increase of the SAR values for lower concentrations of both **1a** and **1b** is observed.

MOA of PTT regarding tumor hypoxia, bio- and nanomaterials applied in PTT show limitations especially concerning biocompatibility, biodegradation, and long-term toxicity.²⁵ Compounds **1a**, **1b**, **2a**, **2b**, **3a**, and **3b** are all small molecules with molecular weights below 600 g/mol, and do not contain any metal atoms. Their nontoxic behavior in HeLa cells in the dark is indicated by an experimental IC_{50} value up to >5 mM. However, upon irradiation these compounds become potent photocytotoxic agents with IC_{50} values as low as 0.0060 ± 0.0003 μM (Table 2), showing that their molecular character overcomes the biocompatibility problems of materials currently applied in PTT.

CONCLUSIONS

The experiments presented have shown that the reported compounds **1a**, **1b**, **2a**, **2b**, **3a**, and **3b** show multiple advantages over established agents for PDT as well as PTT. The novel compounds are easily accessible synthetically and are all metal-free small molecules. They are virtually nontoxic in the dark, which bypasses the biocompatibility/-degradation and toxicity issues found in the applied materials previously used for PTT. SAR determination experiments demonstrate the light-to-heat generation abilities of these compounds, especially of **1b** which shows particularly high SAR values with low concentrations. The

agents are also over 830,000 times more toxic after light activation combined with a photothermal and oxygen-independent MOA (PI of over 360,000 under hypoxic condition of 0.2% O_2), to the best of our knowledge the highest values reported to date (compare with ref 74). In short, these compounds show high potential for overcoming the existing drawbacks of PDT and PTT.

ASSOCIATED CONTENT

Supporting Information

The Supporting Information is available free of charge at <https://pubs.acs.org/doi/10.1021/jacs.2c11650>.

Detailed synthetic procedures; chemical characterization: experimental sections and data; single crystal X-ray measurements: experimental sections and data; photo-physical evaluation: experimental sections and data; biological evaluation: experimental sections and data; computational studies: experimental sections and data; dynamic light scattering: experimental section and data; photothermal evaluation: experimental section and data. (PDF)

AUTHOR INFORMATION

Corresponding Author

Bernhard Spingler – Department of Chemistry, University of Zurich, CH-8057 Zurich, Switzerland; orcid.org/0000-0003-3402-2016; Email: spingler@chem.uzh.ch

Authors

- Lukas Schneider – Department of Chemistry, University of Zurich, CH-8057 Zurich, Switzerland; orcid.org/0000-0003-0052-4560
- Martina Kalt – Department of Chemistry, University of Zurich, CH-8057 Zurich, Switzerland; Institute of Anatomy, University of Zurich, CH-8057 Zurich, Switzerland; Present Address: EAWAG, CH-8600 Dübendorf, Switzerland
- Samuel Koch – Department of Chemistry, University of Zurich, CH-8057 Zurich, Switzerland
- Shanmugi Sithamparanathan – Department of Chemistry, University of Zurich, CH-8057 Zurich, Switzerland
- Veronika Villiger – Department of Chemistry, University of Zurich, CH-8057 Zurich, Switzerland
- Johann Mattiat – Department of Chemistry, University of Zurich, CH-8057 Zurich, Switzerland
- Flavia Kradolfer – Department of Chemistry, University of Zurich, CH-8057 Zurich, Switzerland
- Ekaterina Slyshkina – Department of Chemistry, University of Zurich, CH-8057 Zurich, Switzerland
- Sandra Luber – Department of Chemistry, University of Zurich, CH-8057 Zurich, Switzerland; orcid.org/0000-0002-6203-9379
- Mathias Bonmarin – School of Engineering, Zurich University of Applied Sciences, CH-8400 Winterthur, Switzerland
- Caroline Maake – Institute of Anatomy, University of Zurich, CH-8057 Zurich, Switzerland

Complete contact information is available at: <https://pubs.acs.org/10.1021/jacs.2c11650>

Author Contributions

^{||}L.S. and M.K. contributed equally to the work.

Notes

The authors declare the following competing financial interest(s): M.B. has an equity interest in the company NanoLockin GmbH that may potentially benefit from the research results.

ACKNOWLEDGMENTS

We thank the University of Zurich and the R'Equip programme of the Swiss National Science Foundation (Project Number 206021_164018) for financial support. L.S. was supported by a UZH Forschungskredit grant (Forschungskredit-Beitrag FK-085-19, cofinanced together with the Colbianco Stiftung). We kindly thank Prof. Dr. Roland H. Wenger for providing us with the hypoxia facility and Patrick Spielmann for his help in carrying out the hypoxia experiments. We thank Dr. Thomas Fox for assistance with NMR spectroscopy, Dr. Frank Schumer for synthesizing the APF, Dr. Sabbi Lall from Life Science Editors for valuable comments about our manuscript, and Dr. Jan Helbing, PD Dr. Stefano Ferrari, and Prof. Dr. Pablo Rivera-Fuentes for stimulating discussions. Imaging was performed with support and equipment maintained by the Center for Microscopy and Image Analysis, University of Zurich. FACS experiments were performed with support and equipment maintained by the Cytometry Facility, University of Zurich. The authors would like to acknowledge the company NanoLockin GmbH for providing the Calorsito VIS-NIR device.

REFERENCES

- (1) Zhang, J.; Jiang, C.; Figueiró Longo, J. P.; Azevedo, R. B.; Zhang, H.; Muehlmann, L. A. An updated overview on the development of new photosensitizers for anticancer photodynamic therapy. *Acta Pharm. Sin. B* **2018**, *8* (2), 137–146.
- (2) Lan, M.; Zhao, S.; Liu, W.; Lee, C.-S.; Zhang, W.; Wang, P. Photosensitizers for Photodynamic Therapy. *Adv. Healthcare Mater.* **2019**, *8* (13), 1900132.
- (3) De Silva, P.; Saad, M. A.; Thomsen, H. C.; Bano, S.; Ashraf, S.; Hasan, T. Photodynamic therapy, priming and optical imaging: Potential co-conspirators in treatment design and optimization — a Thomas Dougherty Award for Excellence in PDT paper. *J. Porphyrins Phthalocyanines* **2020**, *24* (11–12), 1320–1360.
- (4) van Straten, D.; Mashayekhi, V.; de Bruijn, H. S.; Oliveira, S.; Robinson, D. J. Oncologic Photodynamic Therapy: Basic Principles, Current Clinical Status and Future Directions. *Cancers* **2017**, *9* (2), 19.
- (5) Agostinis, P.; Berg, K.; Cengel, K. A.; Foster, T. H.; Girotti, A. W.; Gollnick, S. O.; Hahn, S. M.; Hamblin, M. R.; Juzeniene, A.; Kessel, D.; Korbelik, M.; Moan, J.; Mroz, P.; Nowis, D.; Piette, J.; Wilson, B. C.; Golab, J. Photodynamic Therapy of Cancer: An Update. *CA Cancer J. Clin* **2011**, *61* (4), 250–281.
- (6) Yanovsky, R. L.; Bartenstein, D. W.; Rogers, G. S.; Isakoff, S. J.; Chen, S. T. Photodynamic therapy for solid tumors: A review of the literature. *Photodermatol. Photoimmunol. Photomed.* **2019**, *35* (5), 295–303.
- (7) Abrahamse, H.; Hamblin, M. R. New photosensitizers for photodynamic therapy. *Biochem. J.* **2016**, *473*, 347–364.
- (8) Herman, T. S.; Teicher, B. A.; Collins, L. S. Effect of Hypoxia and Acidosis on the Cytotoxicity of 4 Platinum Complexes at Normal and Hyperthermic Temperatures. *Cancer Res.* **1988**, *48* (9), 2342–2347.
- (9) Brown, J. M. Tumor Hypoxia in Cancer Therapy. *Methods Enzymol.* **2007**, *435*, 295–321.
- (10) Baptista, M. S.; Cadet, J.; Di Mascio, P.; Ghogare, A. A.; Greer, A.; Hamblin, M. R.; Lorente, C.; Nunez, S. C.; Ribeiro, M. S.; Thomas, A. H.; Vignoni, M.; Yoshimura, T. M. Type I and Type II Photosensitized Oxidation Reactions: Guidelines and Mechanistic Pathways. *Photochem. Photobiol.* **2017**, *93* (4), 912–919.
- (11) Pucelik, B.; Sulek, A.; Barzowska, A.; Dąbrowski, J. M. Recent advances in strategies for overcoming hypoxia in photodynamic therapy of cancer. *Cancer Lett.* **2020**, *492*, 116–135.
- (12) Hong, L.; Li, J.; Luo, Y.; Guo, T.; Zhang, C.; Ou, S.; Long, Y.; Hu, Z. Recent Advances in Strategies for Addressing Hypoxia in Tumor Photodynamic Therapy. *Biomolecules* **2022**, *12* (1), 81.
- (13) Wilson, B. C.; Patterson, M. S. The physics, biophysics and technology of photodynamic therapy. *Phys. Med. Biol.* **2008**, *53* (9), R61–R109.
- (14) Gál, D. Effect of photosensitizers in chemical and biological processes: The MTO mechanism in photodynamic therapy. *Biochem. Biophys. Res. Commun.* **1992**, *186* (2), 1032–1036.
- (15) Vidóczy, T.; Elzemzam, S.; Gál, D. Physico-chemical modeling of the role of free radicals in photodynamic therapy. I. Utilization of quantum yield data of singlet oxygen formation for the study of the interaction between excited photosensitizer and stable free radicals. *Biochem. Biophys. Res. Commun.* **1992**, *189* (3), 1548–1552.
- (16) Kriska, T.; Jakus, J.; Keszler, A.; Vanyur, R.; Nemeth, A.; Gal, D. Type III photosensitization: attempt for quantification and a way toward new sensitizers. *Proc. SPIE* **1999**, *3563*, 11–17.
- (17) Gal, D.; Kriska, T.; Shutova, T.; Nemeth, A. Additional approach to PDT: type III mechanism and the role of native free radicals. *Proc. SPIE* **2001**, *4248*, 169–178.
- (18) Scherer, K. M.; Bisby, R. H.; Botchway, S. W.; Parker, A. W. New Approaches to Photodynamic Therapy from Types I, II and III to Type IV Using One or More Photons. *Anti-Cancer Agents Med. Chem.* **2017**, *17* (2), 171–189.
- (19) Yoon, I.; Li, J. Z.; Shim, Y. K. Advance in Photosensitizers and Light Delivery for Photodynamic Therapy. *Clin. Endosc.* **2013**, *46* (1), 7–23.
- (20) Smith, G.; McGimpsey, W. G.; Lynch, M. C.; Kochevar, I. E.; Redmond, R. W. An Efficient Oxygen Independent Two-Photon Photosensitization Mechanism. *Photochem. Photobiol.* **1994**, *59* (2), 135–139.
- (21) Dall'Acqua, F.; Martelli, P. Photosensitizing action of furocoumarins on membrane components and consequent intracellular events. *J. Photochem. Photobiol., B* **1991**, *8* (3), 235–254.
- (22) Hamblin, M. R.; Abrahamse, H. Oxygen-Independent Antimicrobial Photoinactivation: Type III Photochemical Mechanism? *Antibiotics* **2020**, *9* (2), 53.
- (23) Huang, H. Y.; Banerjee, S.; Qiu, K. Q.; Zhang, P. Y.; Blacque, O.; Malcomson, T.; Paterson, M. J.; Clarkson, G. J.; Staniforth, M.; Stavros, V. G.; Gasser, G.; Chao, H.; Sadler, P. J. Targeted photoredox catalysis in cancer cells. *Nat. Chem.* **2019**, *11* (11), 1041–1048.
- (24) Li, M.; Gebremedhin, K. H.; Ma, D.; Pu, Z.; Xiong, T.; Xu, Y.; Kim, J. S.; Peng, X. Conditionally Activatable Photoredox Catalysis in Living Systems. *J. Am. Chem. Soc.* **2022**, *144* (1), 163–173.
- (25) Wei, W.; Zhang, X.; Zhang, S.; Wei, G.; Su, Z. Biomedical and bioactive engineered nanomaterials for targeted tumor photothermal therapy: A review. *Mater. Sci. Eng., C* **2019**, *104*, 109891.
- (26) Jung, H. S.; Verwilt, P.; Sharma, A.; Shin, J.; Sessler, J. L.; Kim, J. S. Organic molecule-based photothermal agents: an expanding photothermal therapy universe. *Chem. Soc. Rev.* **2018**, *47* (7), 2280–2297.
- (27) Anand, S.; Chan, T. A.; Hasan, T.; Maytin, E. V. Current Prospects for Treatment of Solid Tumors via Photodynamic, Photothermal, or Ionizing Radiation Therapies Combined with Immune Checkpoint Inhibition (A Review). *Pharmaceuticals* **2021**, *14* (5), 447.
- (28) Su, M.; Han, Q.; Yan, X.; Liu, Y.; Luo, P.; Zhai, W.; Zhang, Q.; Li, L.; Li, C. A Supramolecular Strategy to Engineering a Non-photobleaching and Near-Infrared Absorbing Nano-J-Aggregate for Efficient Photothermal Therapy. *ACS Nano* **2021**, *15* (3), 5032–5042.
- (29) He, Z.; Zhao, L.; Zhang, Q.; Chang, M.; Li, C.; Zhang, H.; Lu, Y.; Chen, Y. An Acceptor–Donor–Acceptor Structured Small Molecule for Effective NIR Triggered Dual Phototherapy of Cancer. *Adv. Funct. Mater.* **2020**, *30* (16), 1910301.
- (30) Li, X.; Fang, F.; Sun, B.; Yin, C.; Tan, J.; Wan, Y.; Zhang, J.; Sun, P.; Fan, Q.; Wang, P.; Li, S.; Lee, C.-S. Near-infrared small molecule

coupled with rigidity and flexibility for high-performance multimodal imaging-guided photodynamic and photothermal synergistic therapy. *Nanoscale Horiz.* **2021**, *6* (2), 177–185.

(31) Huang, S.; Kannadorai, R. K.; Chen, Y.; Liu, Q.; Wang, M. A narrow-bandgap benzobisthiadiazole derivative with high near-infrared photothermal conversion efficiency and robust photostability for cancer therapy. *Chem. Commun.* **2015**, *51* (20), 4223–4226.

(32) Naik, A.; Rubbiani, R.; Gasser, G.; Spingler, B. Visible-Light-Induced Annihilation of Tumor Cells with Platinum–Porphyrin Conjugates. *Angew. Chem. Int. Ed.* **2014**, *53* (27), 6938–6941.

(33) Antoni, P. M.; Naik, A.; Albert, I.; Rubbiani, R.; Gupta, S.; Ruiz-Sanchez, P.; Munikorn, P.; Mateos, J. M.; Luginbuehl, V.; Thamyonkit, P.; Ziegler, U.; Gasser, G.; Jeschke, G.; Spingler, B. (Metallo)porphyrins as Potent Phototoxic Anti-Cancer Agents after Irradiation with Red Light. *Chem.—Eur. J.* **2015**, *21* (3), 1179–1183.

(34) Wu Klingler, W.; Giger, N.; Schneider, L.; Babu, V.; König, C.; Spielmann, P.; Wenger, R. H.; Ferrari, S.; Spingler, B. Low-Dose Near-Infrared Light-Activated Mitochondria-Targeting Photosensitizers for PDT Cancer Therapy. *Int. J. Mol. Sci.* **2022**, *23* (17), 9525.

(35) Hao, E.; Xu, Y.; Yu, C.; Jiao, L. Near-infrared 4-difluoro-4-borata-3a-azonia-4a-aza-s-indacene fluorescent dye and preparation method thereof. CN103952001B, 2014.

(36) Padrutt, R.; Babu, V.; Klingler, S.; Kalt, M.; Schumer, F.; Anania, M. I.; Schneider, L.; Spingler, B. Distyryl-BODIPY-Transplatin Conjugates as Highly Phototoxic Photosensitizers for Photodynamic Therapy. *ChemMedChem* **2021**, *16* (4), 694–701.

(37) Xiao, Y.-F.; Chen, J.-X.; Chen, W.-C.; Zheng, X.; Cao, C.; Tan, J.; Cui, X.; Yuan, Z.; Ji, S.; Lu, G.; Liu, W.; Wang, P.; Li, S.; Lee, C.-S. Achieving high singlet-oxygen generation by applying the heavy-atom effect to thermally activated delayed fluorescent materials. *Chem. Commun.* **2021**, *57* (40), 4902–4905.

(38) Jiang, X.-J.; Lau, J. T. F.; Wang, Q.; Ng, D. K. P.; Lo, P.-C. pH- and Thiol-Responsive BODIPY-Based Photosensitizers for Targeted Photodynamic Therapy. *Chem.—Eur. J.* **2016**, *22* (24), 8273–8281.

(39) Schneider, L.; Larocca, M.; Wu, W.; Babu, V.; Padrutt, R.; Slyshkina, E.; König, C.; Ferrari, S.; Spingler, B. Exocyclicly metallated tetrapyrrolineporphyrin as a potential photosensitizer for photodynamic therapy. *Photochem. Photobiol. Sci.* **2019**, *18* (11), 2792–2803.

(40) Rubbiani, R.; Wu, W.; Naik, A.; Larocca, M.; Schneider, L.; Padrutt, R.; Babu, V.; König, C.; Hinger, D.; Maake, C.; Ferrari, S.; Gasser, G.; Spingler, B. Studying the cellular distribution of highly phototoxic platinumated metalloporphyrins by isotope labelling. *Chem. Commun.* **2020**, *56* (92), 14373–14376.

(41) Le, N. A.; Babu, V.; Kalt, M.; Schneider, L.; Schumer, F.; Spingler, B. Photo-stable platinumated bacteriochlorins as potent photodynamic agents. *J. Med. Chem.* **2021**, *64* (10), 6792–6801.

(42) Schneider, L.; Kalt, M.; Larocca, M.; Babu, V.; Spingler, B. Potent PBS-Soluble Transplatin Derived Porphyrin-Based Photosensitizer for Photodynamic Therapy. *Inorg. Chem.* **2021**, *60* (13), 9416–9426.

(43) Rurack, K.; Kollmannsberger, M.; Daub, J. Molecular Switching in the Near Infrared (NIR) with a Functionalized Boron–Dipyromethene Dye. *Angew. Chem. Int. Ed.* **2001**, *40* (2), 385–387.

(44) Baruah, M.; Qin, W.; Flors, C.; Hofkens, J.; Vallée, R. A. L.; Beljonne, D.; Van der Auweraer, M.; De Borggraeve, W. M.; Boens, N. Solvent and pH dependent fluorescent properties of a dimethylaminostyryl borondipyromethene dye in solution. *J. Phys. Chem. A* **2006**, *110* (18), 5998–6009.

(45) Deniz, E.; Isbasar, G. C.; Bozdemir, Ö. A.; Yildirim, L. T.; Siemiarz, A.; Akkaya, E. U. Bidirectional Switching of Near IR Emitting Boradiazaindene Fluorophores. *Org. Lett.* **2008**, *10* (16), 3401–3403.

(46) Pucelik, B.; Paczynski, R.; Dubin, G.; Pereira, M. M.; Arnaut, L. G.; Dabrowski, J. M. Properties of halogenated and sulfonated porphyrins relevant for the selection of photosensitizers in anticancer and antimicrobial therapies. *PLoS One* **2017**, *12* (10), e0185984.

(47) Becke, A. D. Density-functional exchange-energy approximation with correct asymptotic behavior. *Phys. Rev. A* **1988**, *38* (6), 3098–3100.

(48) Lee, C.; Yang, W.; Parr, R. G. Development of the Colle-Salvetti correlation-energy formula into a functional of the electron density. *Phys. Rev. B* **1988**, *37* (2), 785–789.

(49) Becke, A. D. Density-functional thermochemistry. III. The role of exact exchange. *J. Chem. Phys.* **1993**, *98* (7), 5648–5652.

(50) Stephens, P. J.; Devlin, F. J.; Chabalowski, C. F.; Frisch, M. J. Ab Initio Calculation of Vibrational Absorption and Circular Dichroism Spectra Using Density Functional Force Fields. *J. Chem. Phys.* **1994**, *98* (45), 11623–11627.

(51) Martin, R. L. Natural transition orbitals. *J. Chem. Phys.* **2003**, *118* (11), 4775–4777.

(52) Klamt, A.; Schüürmann, G. COSMO: a new approach to dielectric screening in solvents with explicit expressions for the screening energy and its gradient. *J. Chem. Soc., Perkin Trans.* **1993**, *2* (5), 799–805.

(53) Zorlu, Y.; Dumoulin, F.; Durmuş, M.; Ahsen, V. Comparative studies of photophysical and photochemical properties of solketal substituted platinum(II) and zinc(II) phthalocyanine sets. *Tetrahedron* **2010**, *66* (17), 3248–3258.

(54) Karges, J.; Kuang, S.; Maschietto, F.; Blacque, O.; Ciofini, I.; Chao, H.; Gasser, G. Rationally designed ruthenium complexes for 1- and 2-photon photodynamic therapy. *Nat. Commun.* **2020**, *11*, 3262.

(55) Friedrich, J.; Seidel, C.; Ebner, R.; Kunz-Schughart, L. A. Spheroid-based drug screen: considerations and practical approach. *Nat. Prot.* **2009**, *4* (3), 309–324.

(56) Muz, B.; de la Puente, P.; Azab, F.; Azab, A. K. The role of hypoxia in cancer progression, angiogenesis, metastasis, and resistance to therapy. *Hypoxia* **2015**, *3*, 83–92.

(57) Li, C.; Yu, M.; Sun, Y.; Wu, Y.; Huang, C.; Li, F. A Nonemissive Iridium(III) Complex That Specifically Lights-Up the Nuclei of Living Cells. *J. Am. Chem. Soc.* **2011**, *133* (29), 11231–11239.

(58) Lazarenko, R. M.; DelBove, C. E.; Strothman, C. E.; Zhang, Q. Ammonium chloride alters neuronal excitability and synaptic vesicle release. *Sci. Rep.* **2017**, *7* (1), 5061.

(59) Harper, J. N.; Wright, S. H. Multiple mechanisms of ligand interaction with the human organic cation transporter, OCT2. *Am. J. Physiol. Renal Phys.* **2013**, *304* (1), F56–F67.

(60) Ricci, J.-E.; Muñoz-Pinedo, C.; Fitzgerald, P.; Bailly-Maitre, B.; Perkins, G. A.; Yadava, N.; Scheffler, I. E.; Ellisman, M. H.; Green, D. R. Disruption of Mitochondrial Function during Apoptosis Is Mediated by Caspase Cleavage of the p75 Subunit of Complex I of the Electron Transport Chain. *Cell* **2004**, *117* (6), 773–786.

(61) Skulachev, V. P. Bioenergetic aspects of apoptosis, necrosis and mitoptosis. *Apoptosis* **2006**, *11* (4), 473–485.

(62) Vermes, I.; Haanen, C.; Steffens-Nakken, H.; Reutelingsperger, C. A novel assay for apoptosis Flow cytometric detection of phosphatidylserine expression on early apoptotic cells using fluorescein labelled Annexin V. *J. Immunol. Methods* **1995**, *184* (1), 39–51.

(63) Vermes, I.; Haanen, C.; Reutelingsperger, C. Flow cytometry of apoptotic cell death. *J. Immunol. Methods* **2000**, *243* (1), 167–190.

(64) Darzynkiewicz, Z.; Bruno, S.; Del Bino, G.; Gorczyca, W.; Hotz, M. A.; Lassota, P.; Traganos, F. Features of apoptotic cells measured by flow cytometry. *Cytometry* **1992**, *13* (8), 795–808.

(65) Hemelaar, S. R.; Nagl, A.; Bigot, F.; Rodríguez-García, M. M.; de Vries, M. P.; Chipaux, M.; Schirhagl, R. The interaction of fluorescent nanodiamond probes with cellular media. *Microchim. Acta* **2017**, *184* (4), 1001–1009.

(66) Steinmetz, L.; Kirsch, C.; Geers, C.; Petri-Fink, A.; Bonmarin, M. Investigating a Lock-In Thermal Imaging Setup for the Detection and Characterization of Magnetic Nanoparticles. *Nanomaterials* **2020**, *10* (9), 1665.

(67) Shirata, C.; Kaneko, J.; Inagaki, Y.; Kokudo, T.; Sato, M.; Kiritani, S.; Akamatsu, N.; Arita, J.; Sakamoto, Y.; Hasegawa, K.; Kokudo, N. Near-infrared photothermal/photodynamic therapy with indocyanine green induces apoptosis of hepatocellular carcinoma cells through oxidative stress. *Sci. Rep.* **2017**, *7* (1), 13958.

(68) Machalkova, K.; Skorpikova, J.; Svihalek, J.; Mornstein, V. The study of cytotoxicity and phototoxicity of indocyanine green in vitro. *Scr. Med.* **2005**, *78* (5), 305–312.

(69) Calixto, G. M. F.; Bernegossi, J.; de Freitas, L. M.; Fontana, C. R.; Chorilli, M. Nanotechnology-Based Drug Delivery Systems for Photodynamic Therapy of Cancer: A Review. *Molecules* **2016**, *21* (3), 342.

(70) Larue, L.; Myrzakhmetov, B.; Ben-Mihoub, A.; Moussaron, A.; Thomas, N.; Arnoux, P.; Baros, F.; Vanderesse, R.; Acherar, S.; Frochot, C. Fighting Hypoxia to Improve PDT. *Pharmaceuticals* **2019**, *12* (4), 163.

(71) Gunaydin, G.; Gedik, M. E.; Ayan, S. Photodynamic Therapy—Current Limitations and Novel Approaches. *Front. Chem.* **2021**, *9*, 691697.

(72) Bian, W.; Wang, Y.; Pan, Z.; Chen, N.; Li, X.; Wong, W.-L.; Liu, X.; He, Y.; Zhang, K.; Lu, Y.-J. Review of Functionalized Nanomaterials for Photothermal Therapy of Cancers. *ACS Appl. Nano Mater.* **2021**, *4* (11), 11353–11385.

(73) Tian, B.; Wang, C.; Zhang, S.; Feng, L.; Liu, Z. Photothermally Enhanced Photodynamic Therapy Delivered by Nano-Graphene Oxide. *ACS Nano* **2011**, *5* (9), 7000–7009.

(74) Cole, H. D.; Roque, J. A.; Shi, G.; Lifshits, L. M.; Ramasamy, E.; Barrett, P. C.; Hodges, R. O.; Cameron, C. G.; McFarland, S. A. Anticancer Agent with Inexplicable Potency in Extreme Hypoxia: Characterizing a Light-Triggered Ruthenium Ubertoxin. *J. Am. Chem. Soc.* **2022**, *144* (22), 9543–9547.

Recommended by ACS

Molecular Engineering of pH-Responsive NIR Oxazine Assemblies for Evoking Tumor Ferroptosis via Triggering Lysosomal Dysfunction

Wei Li, Xiao-Bing Zhang, *et al.*

FEBRUARY 02, 2023

JOURNAL OF THE AMERICAN CHEMICAL SOCIETY

READ 

Supramolecular Photosensitizer Enables Oxygen-Independent Generation of Hydroxyl Radicals for Photodynamic Therapy

Kun-Xu Teng, Qing-Zheng Yang, *et al.*

FEBRUARY 13, 2023

JOURNAL OF THE AMERICAN CHEMICAL SOCIETY

READ 

Red-Shifted Coumarin Luciferins for Improved Bioluminescence Imaging

Anna C. Love, Jennifer A. Prescher, *et al.*

FEBRUARY 06, 2023

JOURNAL OF THE AMERICAN CHEMICAL SOCIETY

READ 

Turning Red without Feeling Embarrassed—Xanthenum-Based Photocages for Red-Light-Activated Phototherapeutics

Alexandra Egyed, Márton Bojtár, *et al.*

FEBRUARY 08, 2023

JOURNAL OF THE AMERICAN CHEMICAL SOCIETY

READ 

Get More Suggestions >